

On the theory of magnetar QPOs.

Yuri Levin^{1,2}

¹*Leiden University, Leiden Observatory, P.O. Box 9513, NL-2300 RA Leiden*

²*Leiden University, Lorentz Institute, P.O. Box 9506, NL-2300 RA Leiden*

printed 10 April 2018

ABSTRACT

We consider torsional oscillations of magnetars. This problem features rich dynamics due to the strong interaction between the normal modes of a magnetar’s crust and a continuum of Magneto-Hydro-Dynamic (MHD) modes in its fluid core. We study the dynamics using a simple model of a magnetar possessing a uniform magnetic field and a thin spherical crust. Firstly, we show that global torsional modes only exist when one introduces unphysically large dissipative terms into the equations of motion; thus global modes are not helpful for understanding the magnetar Quasi-Periodic Oscillations (QPOs). Secondly, we solve the initial-value problem by simulating the sudden release of an initially strained crust and monitoring the subsequent crustal motion. We find that the crustal torsional modes quickly exchange their energy with the MHD continuum in the core, and decay by several orders of magnitude over the course of ~ 10 oscillation periods. After the initial rapid decay, the crustal motion is stabilized and several time-varying QPOs are observed. The dynamical spectrum of the simulated crustal motion is in qualitative agreement with that of the x-ray light-curve in the tail of a giant magnetar flare. The asymptotic frequencies of some of the QPOs are associated with the special spectral points—the turning points or edges—of the MHD continuum, and are not related to those of the crust. The observed steady low-frequency QPO at 18 Hz is almost certainly associated with the lowest frequency of the MHD continuum, or its first overtone. We also find that drifting QPOs get amplified when they come near the frequencies of the crustal modes. This explains why some of the observed QPOs have frequencies close to the expected crustal frequencies, and why these QPOs are highly variable with time.

1 INTRODUCTION

Magnetar oscillations have recently been the subject of intense theoretical interest. This interest is motivated by quasi-periodic x-ray luminosity oscillations (QPOs), which were observed in the tails of 2 giant Soft Gamma-ray Repeaters’ (SGR) flares (Israel et al. 2005, Strohmayer & Watts 2005, 2006, Watts & Strohmayer 2006, see also Barat et al. 1983). The QPOs typically last for ~ 100 seconds, are detected with high signal-to-noise ratios, and have frequencies which range from 18 to 1800 Hz. The QPOs open an exciting possibility to directly explore the physics of magnetars, and their correct interpretation is of great importance.

SGR QPOs have been commonly interpreted as pure crustal shear modes (Duncan 1998, Piro 2005, Lee 2006, Samuelsson & Andersson 2006, Watts & Reddy 2006, Sotani et al. 2006a). If this interpretation were correct, it would allow one to measure or strongly constrain the shear modulus and depth of the crust, an unprecedented feat in the neutron-star astrophysics (Strohmayer & Watts 2006). However, the presence of the strong magnetic field which exists inside a magnetar may present difficulties for this interpretation. In particular, Levin (2006, L06) has pointed out that hydro-magnetic (MHD) mechanical coupling between the crust and

the core occurs on the timescale < 0.1 seconds, and should be taken into account. L06 made 2 basic points: 1. MHD coupling ensures that pure crustal modes do not exist, and global modes of the whole star must be considered, and 2. Long-term survival of the global mode is in danger, since it is expected to couple to a continuum of MHD modes (the Alfven continuum) in the core, and this coupling would act to damp the mode. More recently, Glampedakis, Samuelsson, & Andersson 2006 (GSA) and Sotani et al. 2006b (S06b) have found global MHD-elastic modes in simple toy magnetar models, and have argued that the analogues of these modes produce QPOs in real magnetars. However, both of the toy models have been constructed in a way which explicitly excludes the presence of an Alfven continuum in the core^{*}.

^{*} GSA make use of the rectangular geometry with a uniform magnetic field, which ensures that all of the Alfven modes with the same quantum number have the same frequency. S06b consider dipole magnetic field in the spherical magnetar, but explicitly exclude $l \pm 2$ coupling in their equations. This enforces the spherical symmetry in the physical problem described by their equations of motion. In fact, their equations are identical to those that describe oscillation of the star with a purely radial spherically sym-

The coupling of hydrodynamical waves to Alfvén continuum has been extensively studied in the context of solar corona, and is well understood (Ionson 1978, Hollweg 1987a,b). The absorption of the waves by Alfvén continuum is sometimes referred to as the *resonant absorption*. In this paper we build on the work done by the solar physics community and undertake a thorough investigation of the influence of the Alfvén continuum on the oscillatory behavior of the magnetar crust. The plan of the paper is as follows:

In the next section we describe our simplified, but topologically correct magnetar model. We derive equations of torsional motion, and search for normal modes of the system. We find the normal modes only exist if one introduces sufficiently large frictional forces, e.g. the ones of the form $-\gamma d\vec{r}/dt$, into the equations of motion. The eigenfrequencies are complex, and the modes decay with the rate independent of γ , typically over several oscillation periods (i.e., a fraction of a second). However, the normal-mode analysis is inconclusive, since the real frictional forces in a magnetar may be small and the normal modes likely do not exist. Thus in section 3 we turn to the initial value problem. We model the continuum by 10^4 oscillators chosen to mimic closely the MHD dynamics of the core (one can think of this idea as similar to the one behind spectral codes in fluid dynamics, except that our equations are linear. The true linear behavior of the real magnetar is recovered when the number of oscillators tends to infinity). We begin the simulations by releasing an initially strained crust, and then monitor its motion. The result of one such simulation is shown in Fig. 9. We find that the crustal deformation energy is quickly converted into the energy of MHD continuum in the core, as was predicted in L06 and as is suggested by the large imaginary components of the normal-mode frequencies obtained in section 2. The amplitude of crustal motion is reduced by 10^2 over several oscillation periods, but is then stabilized as the crust reacts to the vigorously-moving core. **In this second time-interval we find QPOs in the crustal motion**, see Fig. 10. The asymptotic frequencies of some of the QPOs are associated with the special spectral points of the continuum. Both turning points and edges of the continuum produce QPOs (see section 3 and Figure 4 for an explanation of what these are). We also find that when the frequency of a drifting QPO approaches that of a crustal mode, the QPOs amplitude gets significantly amplified. Thus crustal frequencies feature intermittently enhanced power, in agreement with the observations.

In section 4 we present an outlook on the outstanding theoretical questions related to magnetar QPOs.

metric magnetic field, and thus, just as in GSA, the local Alfvén waves with the same quantum numbers have the same frequency. We note that Rincon & Rieutord (2003) and Reese, Rincon, & Rieutord (2004) have previously found a continuum of torsional modes in the MHD configuration identical to that in S06b (they have not used any simplifying approximations in their analysis). To sum up, in both GSA and S06b the symmetry of their toy models collapses the Alfvén continuum onto the discrete set of frequencies.

2 BASIC MODEL AND ITS NORMAL MODES.

Finding oscillatory modes of magnetic stars presents a formidable computational and conceptual problem. Rincon & Rieutord (2003) and Reese, Rincon, & Rieutord (2004) in a tour-de-force calculation have computed normal modes of an incompressible fluid shell threaded with a dipole magnetic field. Partly motivated by their work, we choose a simple magnetar model, with several basic assumptions: 1. We take the elastic crust to be thin compared to the core size. This is an excellent approximation for mode frequencies less than $\sim 600\text{Hz}$. 2. We assume that the fluid core has uniform density and is threaded by a homogeneous internal magnetic field directed along the z -axis. This assumption does not change the physics of the problem, but does simplify the calculations and makes them more transparent.

We also consider oscillations with purely azimuthal, ϕ -independent displacements ξ and $\bar{\xi}$ of the core and the crust, respectively:

$$\begin{aligned}\xi_r &= \xi_\theta = \bar{\xi}_r = \bar{\xi}_\theta = 0, \\ \xi_\phi &= \xi_\phi(r, \theta), \\ \bar{\xi}_\phi &= \bar{\xi}_\phi(\theta)\end{aligned}\tag{1}$$

Here r, θ, ϕ are the spherical coordinates. We have made use of the thin-crust assumption in writing the last equation.

We are now in the position to write down equations of motion for small displacements of the crust and the core:

$$\frac{\partial^2 \bar{\xi}_\phi}{\partial t^2} = L_{\text{el}}(\bar{\xi}_\phi) + L_B,\tag{2}$$

$$\frac{\partial^2 \xi_\phi}{\partial t^2} = c_a^2 \left(\frac{\partial^2 \xi_\phi}{\partial z^2} \right)_{r \sin \theta} - \gamma \frac{\partial \xi_\phi}{\partial t}.\tag{3}$$

where the partial derivative on the right-hand side of Eq. (3) is evaluated along the z -direction. Here c_a is the Alfvén velocity, $L_{\text{el}}(\bar{\xi}_\phi)$ and L_B is the acceleration of the crust due to the elastic and magnetic stresses, respectively. We have introduced the frictional term $-\gamma \partial \xi_\phi / \partial t$ into Eq. (3); we will show shortly that this term is needed to regularize the resonant response of the core to the periodic motion of the crust and is crucial for the existence of a normal mode. The expression for L_B is derived below, while that for L_{el} is derived in the Appendix:

$$L_{\text{el}}(\bar{\xi}_\phi) = \omega_{\text{el}}^2 \left[\frac{\partial^2 \bar{\xi}_\phi}{\partial \theta^2} + \cot(\theta) \frac{\partial \bar{\xi}_\phi}{\partial \theta} - (\cot^2(\theta) - 1) \bar{\xi}_\phi \right],\tag{4}$$

where ω_{el} is the frequency given by

$$\omega_{\text{el}} = \frac{\sqrt{\bar{\mu}/\bar{\rho}}}{R},\tag{5}$$

where $\bar{\mu}$ and $\bar{\rho}$ are the vertically averaged shear modulus and density of the crust, respectively, and R is the radius of the star.

2.1 Dynamics of the core: continuum of modes and response to periodic forcing.

It is instructive to consider the motion of the core fluid, with the assumption of a fixed or periodically moving crust as an external boundary condition. The former will elucidate the structure of the Alfvén continuum, while the latter is instrumental in the normal-mode analysis.

Hydro-magnetic stress enforces a no-slip boundary condition at the crust-core interface:

$$\xi_\phi(R, \theta) = \bar{\xi}_\phi. \quad (6)$$

Let us consider the dynamics of the core, with the assumption of a fixed crust and zero friction. The core displays a continuum of singular oscillatory solutions to the pair of equations (3) and (6). These solutions are localized on cylinders of radius η_0 , with $0 < \eta_0 < R$, and their mathematical form is expressed most easily in cylindrical coordinates η, z, ϕ :

$$\xi_\phi(\eta, z, \phi, t) = \delta(\eta - \eta_0) \sin[n\pi z/h(\eta_0)] \times \exp[i\pi n c_a t/h(\eta_0)] \quad (7)$$

or

$$\xi_\phi(\eta, z, \phi, t) = \delta(\eta - \eta_0) \cos[(n + 1/2)\pi z/h(\eta_0)] \times \exp[i\pi n c_a t/h(\eta_0)]; \quad (8)$$

cf. section 3 of L06. Here $h(\eta_0) = \sqrt{R^2 - \eta_0^2}$ is the height of each cylinder, and n is an integer. While this continuum of MHD modes was derived for a simple magnetic-field geometry, it must exist in other field geometries which can be obtained by continuous deformation of the uniform field. Moreover, since a continuous deformation of the field changes the mode frequencies continuously, the topology of the spectrum remains unchanged. This means that the modes will form a countable set of one-dimensional continua; in other words, even for a complicated magnetic-field configuration the mode is parametrized by a pair of real and integer numbers. The latter consideration will become important when we discuss general properties of QPOs in section 3.

Now consider the core's response to a periodic motion of the crust, $\bar{\xi}(\theta) = g(\theta) \exp(i\omega t)$, where ω could, in general, be complex. First we note that the geometry of our problem possesses the reflection symmetry with respect to the $z = 0$ plane. Therefore the normal modes will be either even or odd with respect to z , and we restrict the crustal motion to that with $g(\theta) = \pm g(\pi - \theta)$. From Eqs. (3) and (6), we see that in the “odd” case the core motion is given in cylindrical coordinates by

$$\xi_\phi(\eta, z) = \frac{\sin(kz)}{\sin[kh(\eta)]} \bar{\xi}_\phi[\theta(\eta)], \quad (9)$$

while in the “even” case

$$\xi_\phi(\eta, z) = \frac{\cos(kz)}{\cos[kh(\eta)]} \bar{\xi}_\phi[\theta(\eta)], \quad (10)$$

where $\theta(\eta) = \arcsin(\eta/R)$, $h(\eta) = \sqrt{R^2 - \eta^2}$, and $k = \sqrt{\omega^2 - i\omega\gamma}/c_a$.

2.2 Normal modes

Now we are ready to derive the acceleration of the crust due to the hydromagnetic stress at the crust-core interface:

$$L_B = -\frac{\rho_c c_a^2}{\Sigma} \cos \theta \left(\frac{\partial \xi}{\partial z} \right)_{z=h}, \quad (11)$$

where ρ_c is the density of the fraction of the core fluid which participates in the Alfvén motion, Σ is the column density of the crust, and the partial derivative is evaluated at $(\eta, z) = (R \sin \theta, R \cos \theta)$. By substituting Eq. (9)

or (10) into Eq. (11), we get the following expressions for magnetically-driven acceleration of the crust:

$$L_B(\theta) = -\nu_a \omega_1 \frac{\rho_c R}{\Sigma} \cot(\omega_1 \cos \theta / \nu_a) \cos \theta \bar{\xi}_\phi(\theta) \quad (12)$$

for the odd modes, and

$$L_B(\theta) = \nu_a \omega_1 \frac{\rho_c R}{\Sigma} \tan(\omega_1 \cos \theta / \nu_a) \cos \theta \bar{\xi}_\phi(\theta) \quad (13)$$

for the even modes. Here $\nu_a = c_a/R$, and $\omega_1 = \sqrt{\omega^2 - i\omega\gamma}$.

We can now see that the Eq. (2), together with Eqs. (4) and (12/13), form an ordinary second-order differential equation for $\bar{\xi}_\phi(\theta)$. The values of ω get selected by requiring that the solution of Eq. (2) satisfies the boundary conditions[†] at the poles $\theta = 0, \pi$:

$$\bar{\xi}_\phi(\theta) = \frac{\partial^2 \bar{\xi}_\phi(\theta)}{\partial \theta^2} = 0. \quad (14)$$

We found it practical to solve Eq. (2) in the upper hemisphere, but require that at the equator either $\bar{\xi}_\phi(\theta) = 0$ for the odd modes, or $\partial \bar{\xi}_\phi(\theta)/\partial \theta = 0$ for the even modes. We also found it useful to make the substitution

$$q(\theta) = \bar{\xi}_\phi(\theta)/\theta, \quad (15)$$

and rewrite the equations in terms of $q(\theta)$. The new equations do not have a singularity at the pole $\theta = 0$, and are very easy to integrate on the computer. We have checked the code by solving both analytically and numerically the case with $L_B = 0$. We find analytically that the wavefunctions of the free-crust vibrational modes are given by

$$\bar{\xi}_\phi(\theta) = \partial Y_{l0}(\theta)/\partial \theta, \quad (16)$$

with the eigenfrequencies

$$\omega_l = \sqrt{(l-1)(l+2)} \omega_{e1}. \quad (17)$$

This l -scaling is in full agreement with that of Samuelsson & Andersson (2006). Our numerics gives excellent agreement with these results.

Before we discuss our numerical results for the case of a non-zero L_B , one qualitative remark is due. From Eqs. (12) and (13), we see that if ω is real and the friction coefficient $\gamma = 0$, then L_B diverges for the values of θ which correspond to the location of the Alfvén continuum mode in resonance with ω . It is these resonant interactions that are largely responsible for the exchange of energy between the global vibration and the Alfvén continuum, and that are thus responsible for determining the imaginary part of ω (hence the name “resonant absorption” in the solar literature). In our Runge-Kutta routine, we enforce small θ -steps which scale as L_B^{-2} near the singularities (and we check that our results do not change when the step-size is reduced by a factor of 10).

We now discuss our numerical results for normal modes of a magnetar. We find that the normal modes exist only when γ is sufficiently large, i.e. $\gamma > \gamma_{\text{crit}}$. When this condition is satisfied, then the frequency of the normal mode is complex and the mode decays with the rate close to γ_{crit} . By

[†] These boundary conditions are derived mathematically from the Frobenius series expansion of $\bar{\xi}_\phi(\theta)$ near the poles, or physically by requiring the crustal angular velocity and acceleration be finite at the poles.

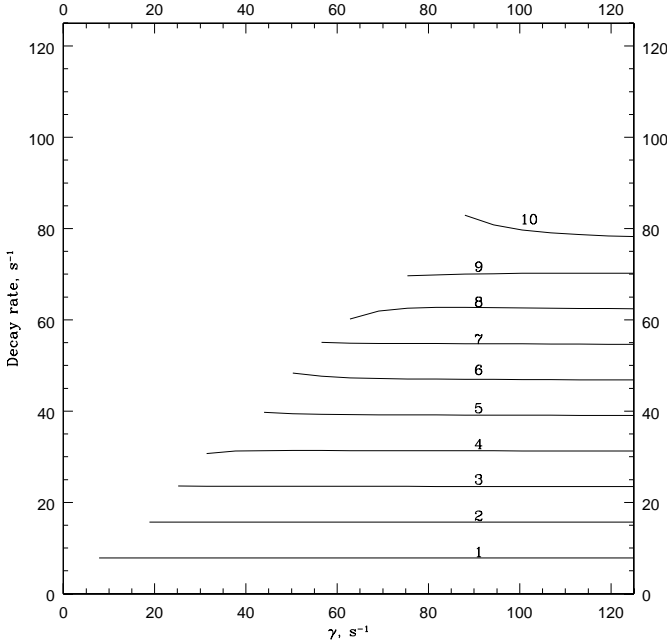


Figure 1. Damping rate for a global torsional mode is plotted as a function of the dissipative rate γ . The lines in the figure are numbered by an integer $i = 1, \dots, 10$; each line corresponds to the magnetic field strength $B_{\text{eff}} = i \times 10^{14} \text{ G}$. For small γ , i.e. to the left of the lines, the modes don't exist.

contrast, when $\gamma < \gamma_{\text{crit}}$, a thorough numerical search fails to identify the complex eigenfrequency for which all of the boundary conditions are satisfied. This is in full agreement with previous work done on the resonant absorption in the solar corona. For example, in Steinolfson's (1985) simulation the system behaves like a decaying normal mode when the friction is sufficiently large, while for small friction no normal-mode-like behaviour occurs and instead, the phase mixing is observed, where individual modes of the continuum are excited and oscillate each at their own frequency. The same occurs in our initial-value simulations, which we describe in Section 3. Hollweg (1987a,b) gives an excellent physical discussion of why, when the mode exists, its decay-rate is friction-independent[‡]

In figure 1 we show the decay rate for the lowest-frequency normal mode as a function of γ , for the ten values magnetic-field strengths $B_{\text{eff}} = \sqrt{4\pi\rho c_a}$ ranging from 10^{14} to 10^{15} Gauss.

[‡] Briefly, this can be understood as follows: the energy is absorbed in narrow resonant layers; in our case they have cylindrical shapes. Friction produces 2 main effects: (a) it reduces the excitation amplitude of the resonant layer, and (b) it increases the effective width of the layer. It is easy to check that for the simple frictional terms we are using, the 2 effects compensate each other and the total absorption power is friction-independent. Hollweg (1987) proves that the same result holds for more complicated dissipative effects, like viscosity or Ohmic dissipation in the plasma.

Here $B_{\text{eff}} = \sqrt{BB_c}$ if the protons form a superconductor with the critical field strength B_c , and B_{eff} if the protons form a normal fermi liquid, and ρ is the density of the core material coupled to the magnetic field[§]. Our fiducial parameters were $\rho R/\Sigma = 10$ [probably an underestimate, but its increase would only increase the crust-core coupling—see Eqs (12) and (13)], $\omega_{\text{el}} = 2\pi \times 20 \text{ Hz}$, and $\nu_a/\omega_{\text{el}} = 0.2$, appropriate for $\rho \sim 10^{14} \text{ g/cm}^3$. We see that when the modes exist they show rapid decay, on the timescale $\ll 1$ second. This result holds for all higher-order modes we have considered, and shows how efficiently the crustal motion is coupled to the continuum. However, the friction (e.g., due to viscosity) may be small in magnetars, and the normal modes most likely do not exist. Thus the problem of magnetar torsional motion must be addressed using initial-value simulations. This is the subject of the next section.

3 INITIAL-VALUE SIMULATIONS

The aim of this section is to simulate torsional motion of a magnetar. During this motion, the discrete torsional modes of the crust interact strongly with a continuum of Alfvén modes in the core, and this interaction affects dramatically the motion of the crust. In the next subsection, we explore with a help of a toy model the dynamics of a harmonic oscillator coupled to a continuum of oscillators. The toy model provides us with an insight into QPOs of such a system, and gives us intuition for what to expect in the case of a magnetar. In subsection 3.2 we set up the initial-value simulation for our magnetar model (the “real” magnetar, as opposed to the toy model in subsection 3.1), and present results.

3.1 Coupling of a harmonic oscillator to a continuum: toy model.

In Figure 2 we show the set-up of our toy problem. We consider a pendulum weighing 1kg, with a proper oscillation angular frequency of $\omega_0 = 1$ (the units are irrelevant). We model the pendulum coupling to a continuum of modes by suspending 10000 tiny pendulae, each weighing 0.01g, from the big pendulum. We arrange the angular frequency of the small pendulae to be

$$\omega_m = 0.5 + .0001 * m, \quad (18)$$

where $m = 1, 2, \dots, 10000$. Thus the frequency of the big pendulum lies in the middle of the range of those of the small

[§] This density can range from the density of protons ρ_{pr} if the neutron superfluid is entirely decoupled from the proton motion, to the full core density ρ_{core} if the neutrons are efficiently coupled to protons. Our guess is that in reality ρ takes the value somewhere in between the 2 extremes: it may be hard for neutron superfluid to become completely decoupled from the charged component, since neutron superfluid vortices are expected to be strongly magnetized and may interact strongly with the superconducting flux-tubes; see, e.g., Ruderman et al. 1998 and references therein. We take the numerical value $\rho = 10^{14} \text{ g/cm}^3$, about 1/10 of the core density and twice the proton density. Our choices for B and ρ affect directly the value of the lowest-frequency QPO simulated in section 3.

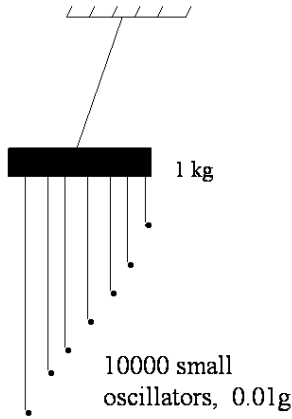


Figure 2. Big pendulum coupled to a large number of small one.

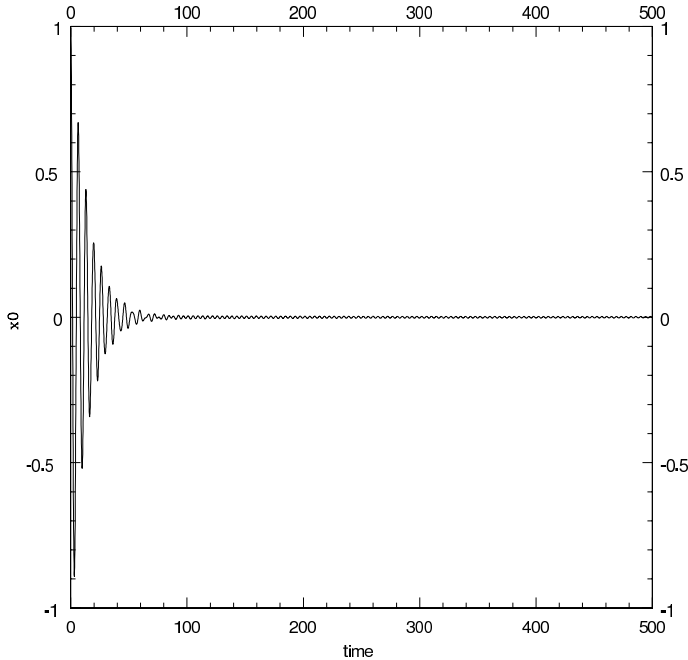


Figure 3. Big-pendulum displacement as a function of time.

pendulae. The initial condition for our simulation is as follows: the big pendulum is deflected by a small angle (we keep the problem linear), while the small pendulae are relaxed and hanging straight down. This is meant to mock an initially strained crust and relaxed core. The big pendulum is released, and the evolution is followed by two independent numerical routines. One routine uses the 4-th order Runge-Kutta method, while the other one uses a symplectic second-order leapfrog algorithm, which is very robust for simulating Hamiltonian systems (see, e.g., Kinoshita, Yoshida, & Nagai 1991). Both runs conserve the total energy of the system with high precision, and produce results which are in excellent agreement with each other. In Fig. 3 we plot the

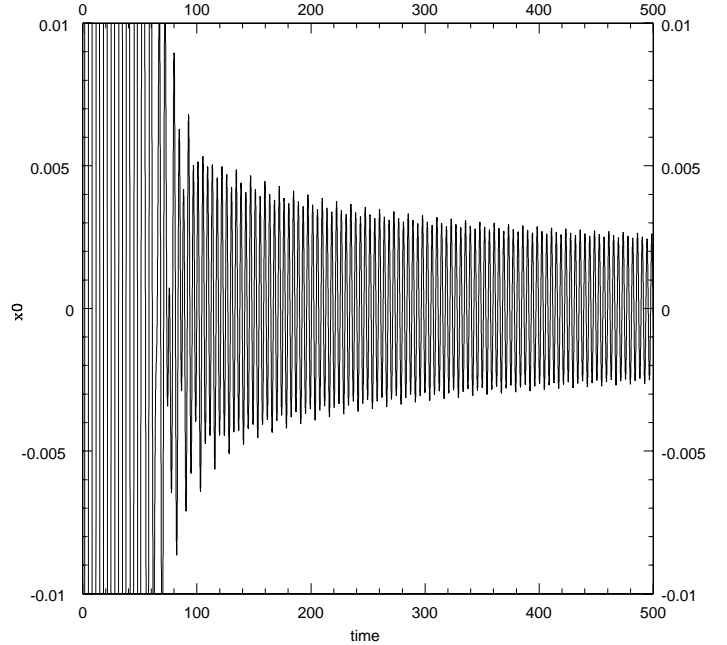


Figure 4. Zoom-in on the post-decay part of Fig. 3. Quasi-periodicity is clearly visible.

big-pendulum displacement as a function of time. After several oscillations, the amplitude of the pendulum’s motion is reduced by ~ 100 , as the energy is rapidly transferred from the big pendulum to the small ones. Then the exponential decay abruptly stops, as the big pendulum now reacts to the collective pull of the small ones. The blow-up of this second region is shown in Fig. 4. The amplitude still decays, but only slowly, as $1/t$. Astonishingly, even with naked eye, one can detect **QPO(s)** in the pendulum motion! Figure 5 shows the time Fourier transform of the big-pendulum displacement for this interval of time. Two QPO frequencies are clearly present, 1.5 and 0.5, both identified with the edges of the continuum and NOT with the natural frequency of the big pendulum!

We get a clue for the origin of these QPOs by plotting the phases of small pendulae as a function of the oscillator frequency, ω_m ; see Figure 6. Over the range of m , the phases average out, thus preventing the small pendulae from pulling coherently on the big pendulum. The only location where this averaging does not occur is near the end points of the spectrum; see the arrows on Figure 6. Thus the pendulae near the end points of the spectrum do pull coherently on the big pendulum and produce the 2 QPOs observed in the simulations. The number of “coherent” oscillators shrinks as $1/t$, as the phase gradients with respect to m grow linearly with time. This explains why the QPO amplitude decays as $1/t$. In Appendix B we present a more mathematical way to understand this phenomenon.

Apart from edges, there may be other special points in the continuum which could generate QPOs. One example is the local maximum or minimum in ω_m as a function of m ; we shall call such special points *the turning points*. The same reasoning as that for the edges, shows that the phases

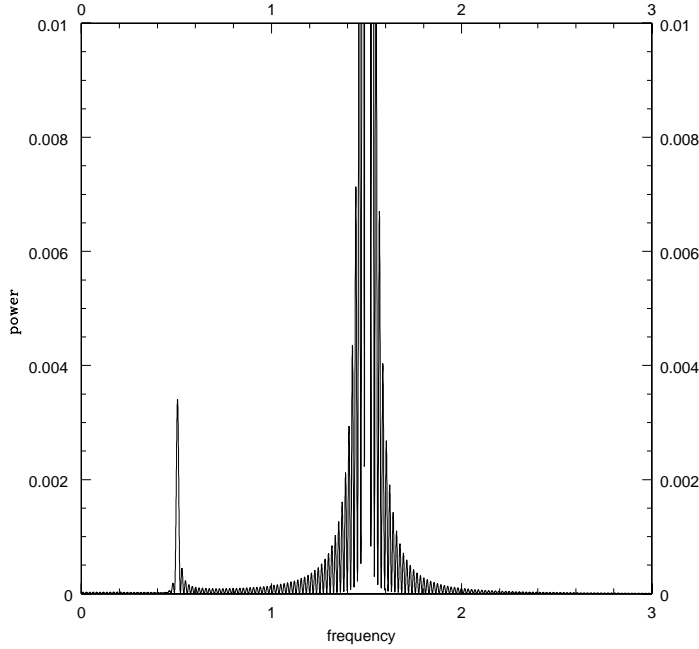


Figure 5. Power spectrum of the post-decay big-pendulum displacement. Two QPOs are clearly visible; they are associated with the edges of the continuum frequency interval.

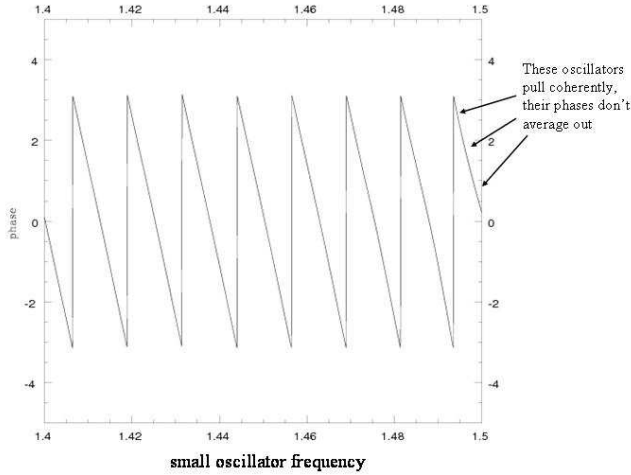


Figure 6. Phases of the small pendulae.

of small oscillators near the turning point will not average out for some time, and hence these oscillators will act coherently. Moreover, the density of states is higher near a turning point than that near an edge, and diverges as $|\omega - \omega_0|^{-1/2}$, where ω_0 is the frequency of the reversal. We thus expect that turning points generate stronger QPOs than the edges; this is confirmed by our simulations shown below. The simulations also show that the turning-point-generated QPOs are longer lived than the edge-generated, and their amplitudes decay only as $t^{-1/2}$. This decay law is explained mathemati-

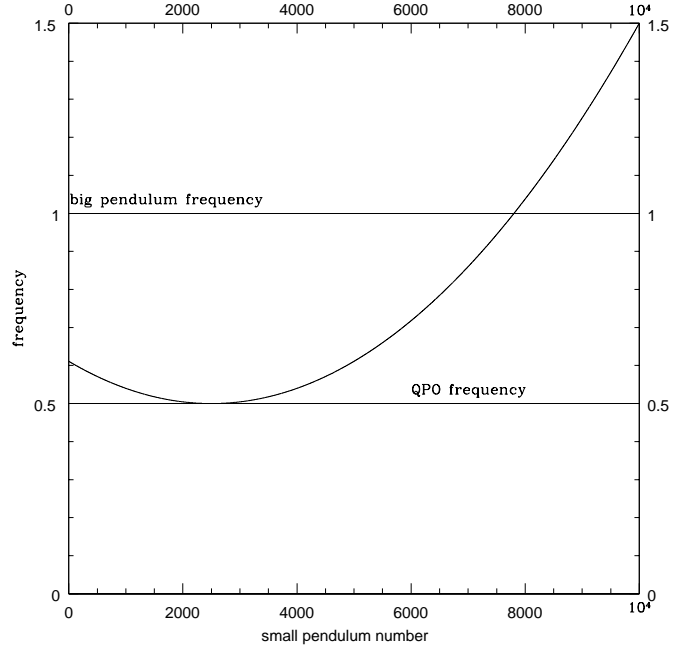


Figure 7. Spectral law with the turning point.

cally in Appendix B. Figure 7 shows an example of a spectral law with a turning point.

We simulate the initial-value problem for this example and show in Fig. 8 the big pendulum's displacement as a function of time. The strong long-lived QPO at the turning-point frequency of 0.5 is apparent with the naked eye.

3.1.0.1 Effect of viscosity. We have modeled the effect of viscosity by introducing frictional forces between neighbouring small oscillators. We expect that with the passage of time the small oscillators get more out of phase, the velocity shear increases and so does the dissipation rate. This is confirmed by our simulations: the total mechanical energy of the system is drained efficiently after some time. In magnetars, this may efficiently heat the core and affect the post-burst afterglow; we shall discuss these issues elsewhere. We find, though, that the QPOs survive for a much longer time than the global mechanical energy, because the oscillators creating it are precisely those ones which are moving in concert. The QPOs generated by the turning points are particularly robust.

3.2 Initial-value problem for the magnetar model

Lessons learned from the toy model lead us to expect (a) rapid decay of initial crustal perturbation and excitation of the core continuum, and (b) QPOs generated by the edges and turning points of this continuum. In our model for the magnetar we have turning points in all Alfvén overtones, at angular frequencies $\omega_n = n\pi c_a/R$ for the odd modes, and $\omega_n = (n - 1/2)\pi c_a/R$ for the even ones; the odd torsional motions are decoupled from the even ones. Thus potentially we expect QPOs at all of these frequencies. We shall find however, that our magnetar model displays a much richer

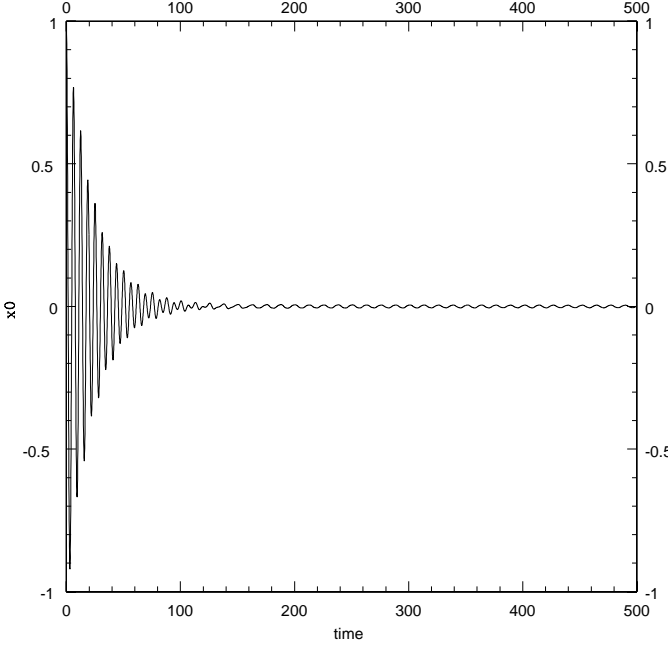


Figure 8. Big-pendulum displacement as a function of time. Here it is calculated for the case when the small pendulae follow the spectral law in Fig. 7. QPO associated with the turning point is clearly visible in the post-decay time interval.

dynamics than the toy models of the previous subsection, although the basic features of the toy models (initial rapid decay of the crustal motion, QPOs associated with continuum turning points) remain. In what follows we explain how our initial-value simulations are set up and show the results.

3.2.0.2 Modal decomposition. A crustal displacement could be represented as a sum of the crustal normal modes:

$$\bar{\xi}_\phi(\theta, t) = \sum_j b_j(t) f_j(\theta), \quad (19)$$

where $f_j(\theta)$ are proportional to the functions given in Eq. (16), and are normalized so that

$$\int_0^\pi f_i(\theta) f_j(\theta) d\theta = \delta_{ij}. \quad (20)$$

We now develop a formalism which allows us to numerically compute the time-evolution of $b_i(t)$. When the crust is not coupled to the core, $b_i(t)$ oscillate harmonically with the frequencies of corresponding crustal modes, but their behaviour is very different when the crustal modes are coupled to the continuum modes in the core. In what follows we model this continuum with a large but finite number of small oscillators, and we test that our results do not change when the number of oscillators is increased.

Consider, for concreteness, only odd modes (they remain decoupled from the even ones because of the reflection symmetry). Recall that for a fixed cylindrical radius η_0 , the equation of motion for the core fluid is

$$\frac{\partial^2 \xi_\phi(\eta_0, z)}{\partial t^2} = c_a^2 \frac{\partial^2 \xi_\phi(\eta_0, z)}{\partial z^2}, \quad (21)$$

with boundary conditions $\xi_\phi(\eta_0, h) = \bar{\xi}_\phi[\theta(\eta_0)]$ and $\xi_\phi(\eta_0, 0) = 0$, where $h = \sqrt{R^2 - \eta_0^2}$ is the cylinder's height, and $\theta(\eta_0) = \arcsin(\eta_0/R)$. Let us introduce a new variable,

$$\chi(\eta_0, z) = \xi_\phi(\eta_0, z) - \bar{\xi}_\phi[\theta(\eta_0)] \frac{z}{h}. \quad (22)$$

We obtain an inhomogeneous equation for χ ,

$$\frac{\partial^2 \chi(\eta_0, z)}{\partial t^2} - c_a^2 \frac{\partial^2 \chi(\eta_0, z)}{\partial z^2} = -\frac{z}{h} \frac{\partial^2 \bar{\xi}_\phi[\theta(\eta_0)]}{\partial t^2}, \quad (23)$$

but with easy boundary conditions

$$\chi(\eta_0, 0) = \chi(\eta_0, h) = 0. \quad (24)$$

Because of this boundary conditions, we can expand χ in a Fourier series:

$$\chi(\eta_0, z, t) = \sum_{n=1}^{\infty} a_n(\eta_0, t) \sin(n\pi \bar{z}), \quad (25)$$

where $\bar{z} = z/h(\eta_0)$. The right-hand side of Eq. (23) can be expanded in the same Fourier basis using the identity

$$\bar{z} = -2 \sum_{n=1}^{\infty} \frac{(-1)^n}{n\pi} \sin(n\pi \bar{z}). \quad (26)$$

Now, by substituting Eqs. (25) and (26) into Eq. (23), we obtain the equations of motion for a_n :

$$\frac{\partial^2 a_n(\eta_0, t)}{\partial t^2} + n^2 \pi^2 \nu_a^2 a_n(\eta_0, t) = \frac{2(-1)^n}{\pi n} \frac{\partial^2 \bar{\xi}_\phi[\theta(\eta_0)]}{\partial t^2}. \quad (27)$$

We now use Eq. (11) to write down the expression for the hydromagnetic backreaction on the crust:

$$L_B(\theta) = -\frac{\rho R}{\Sigma} (c_a/R)^2 \left(\sum_{n=1}^{\infty} n\pi (-1)^n a_n[\eta(\theta)] + \bar{\xi}(\theta) \right). \quad (28)$$

The crustal mode amplitudes $b_m(t)$ obey the following equations of motion:

$$\frac{\partial^2 b_m}{\partial t^2} + \omega_m^2 b_m = \int_0^\pi L_B(\theta) f_m(\theta) \sin \theta d\theta, \quad (29)$$

where ω_m is the frequency of the m 's crustal mode. In writing the last equation, we have used the normalization property of the modal wavefunctions $f_m(\theta)$. So far we have not used any approximations. Now we discretize the integral in Eq. (29) by summing over a large number N of points θ_i , which we take to be equally spaced with the interval $\Delta\theta = \pi/N$. When we do the sum, the continuum mode amplitude $a_n(\theta)$ is substituted with the discrete one, $a_n = a_n(\theta_i)$. Thus effectively doing the sum instead of the integral substitutes a continuum of the core modes with the large number of the discrete core modes. The true continuum dynamics is fully recovered when N goes to infinity.

We are now in the position to write down the equations of motion for the coupled crustal and core modes. From Eq. (27), we have

$$\frac{\partial^2 a_{in}}{\partial t^2} + n^2 \pi^2 \nu_a^2 a_{in} = \frac{2(-1)^n}{\pi n} \sum_{m=1}^{\infty} \frac{\partial^2 b_m(t)}{\partial t^2} f_m(\theta_i). \quad (30)$$

Further, from Eq. (29) we get

$$\begin{aligned} \frac{\partial^2 b_m}{\partial t^2} + \left(\omega_m^2 + \frac{\rho R}{\Sigma} \nu_a^2 \right) b_m = \\ = -\frac{\rho R}{\Sigma} \nu_a^2 \Delta\theta \sum_{n,i} n\pi (-1)^n f_m(\theta_i) \sin \theta_i a_{in}. \end{aligned} \quad (31)$$

Equations (30) and (31) are the main equations of this section. As with our toy models, we integrate these equations using 2 independent numerical techniques, the fourth-order

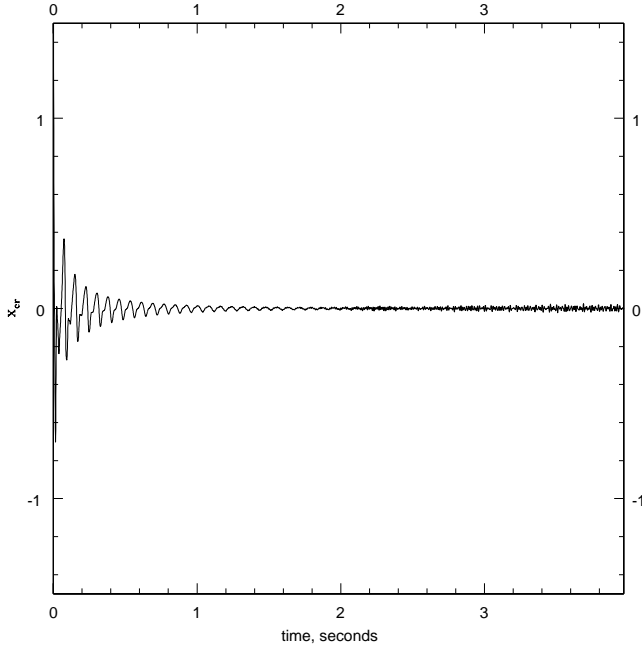


Figure 9. Crust displacement as a function of time.

Runge-Kutta and the second-order leapfrog. The 2 methods give results which are in excellent agreement with each other.

We can now show some results from our numerical experiments. Here, we consider the 2 lowest odd crustal modes, b_1 and b_2 , with frequencies of 40Hz and 84.5Hz, coupled to 10000 odd modes of the continuum: 1000 values of θ_i with 10 Alfvén overtones at each point. This model should be representative for variability below 100Hz. For higher frequencies it is desirable to move away from the thin-crust approximation; this is the subject of future investigations. We begin with the crustal displacement $b_1 = b_2 = 1$ and the relaxed core, $a_{in} = 0$. We monitor the crustal displacement at $\theta = \pi/4$. In Fig. 9 we plot this displacement as a function of time for the first few seconds after release. Like in our toy models, we observe an initially rapid decay of crustal motion, due to pumping of the crustal energy into the core. The crustal motion is then stabilized as the crust reacts to the vigorous movement of the neutron-star core. In Fig. 10 we plot the dynamical spectrum of the crustal motion for the first 100 seconds (we split the time-axis into 1/2-second intervals, and take a Fourier transform at each interval. The density of points represents the magnitude of the square of the Fourier transform). In the dynamical spectrum, we see several QPO-type features. The low-frequency QPOs asymptote to the turning points of the core continuum, $c_a n \pi / R$ (here we are considering the odd modes). Intermittent drifting QPOs appear at higher frequencies, and they get strongly amplified near the crustal frequencies. The nature of the QPO frequency drifts is unclear to us at this point.

The simulated dynamical spectrum of Fig. 10 is in qualitative agreement with that of the x-ray lightcurve in the tail of a giant flare, see Israel et al. 2005. In both cases there is

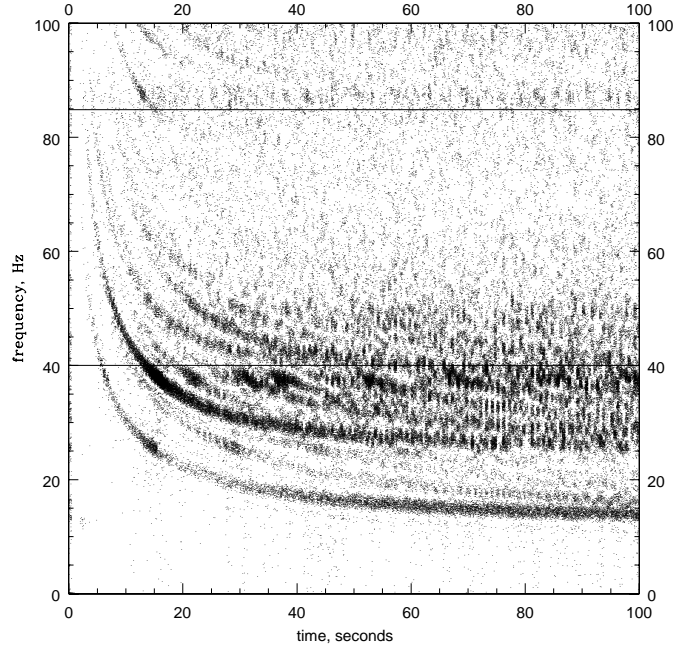


Figure 10. Dynamical spectrum of the crustal displacement. Thin horizontal lines mark the pure crustal frequencies. Two low-frequency QPOs asymptote to the continuum turning points, and are unrelated to the crustal modes. Larger version of the figure, with better resolution near the crustal frequencies, is available upon request.

significant steady power below the lowest crustal frequency, and we conclude that the observed 18Hz QPO is almost certainly the turning point of the core continuum. We also see an intermittent excess of power near the crustal frequencies, in qualitative agreement with the observations.

4 OUTLOOK

In this paper we have elucidated the crucial role that the core Alfvén continuum plays in the dynamics of torsional motion of magnetars. We have shown that the global torsional modes do not exist unless the friction is unphysically large. We have performed a series of initial-value simulations for a simple but geometrically realistic magnetar model, and have observed QPOs with the properties closely resembling those in the tails of giant magnetar flares. In our model, the steady low-frequency QPOs are associated with the turning points of the Alfvén continuum. This gives us a constraint on the combination of magnetic field geometry and strength and density of the core material which is coupled to the magnetic field. For our geometry,

$$\left(\frac{B}{10^{15} \text{G}} \right) \left(\frac{10^{14} \text{g/cm}^3}{\rho} \right)^{1/2} \left(\frac{10 \text{km}}{R} \right) \simeq 1. \quad (32)$$

Some of the higher-frequency power is clustered around the crustal frequencies, in agreement with the observations. This seems to be due to intermittent amplification of the drifting QPOs when they are close to a crustal frequency.

While the qualitative agreement between our simulations and observations is good, we see several directions for future research:

1. Investigate qualitatively the origin of the QPO drifts in the simulations, and the reason why the QPO amplitudes get amplified near the crustal frequencies.
2. Study the Alfvén continuum for more realistic field geometries, e.g. the ones proposed in Braithwaite & Spruit 2004, 2006.
3. Investigate quantitatively the effect of viscous friction in the core. We have done some pilot studies for the toy models in the subsection 3.1, and have found that viscous friction is very efficient in draining of the core's kinetic energy, but does not significantly affect the QPOs. It is interesting to learn whether some of the long-term thermal afterglow could be generated from the heat deposited in the core by viscously damped Alfvén waves.
4. Investigate the dynamics of the magnetosphere. It is likely that the magnetosphere also features the continuum of Alfvén modes, and they will affect the emission of x-rays in the giant flare afterglow.

5 ACKNOWLEDGMENTS

I thank Wim van Saarloos and Henk Spruit for helpful discussions. The final stages of this work were completed at the Australia Telescope National Facility, Sydney, for whose hospitality I am grateful.

6 APPENDIX A: ELASTIC FORCES AND ACCELERATIONS

The purpose of this Appendix is to derive the expression (4) in the text for the crustal acceleration due to elastic forces. Since our problem is axially symmetric, the quickest derivation is obtained by considering the flow of the z -component of the shell's angular momentum density. The displacement $\bar{\xi}_\phi(\theta)$ causes the horizontal shear stress in the shell which is given by:

$$T_{\theta\phi} = (\mu/R) \sin \theta \frac{\partial(\bar{\xi}_\phi(\theta)/\sin \theta)}{\partial \theta}, \quad (33)$$

where μ is the shear modulus of the shell. The flow of angular momentum in the ∂_θ direction is given by

$$L_{\text{flux}} = 2\pi(R \sin \theta)^2 \int dr T_{\theta\phi}, \quad (34)$$

where the integration is over the thickness of the shell. The small thickness of the shell warrants the assumption of r -independent $\bar{\xi}_\phi(\theta)$, so only μ needs to be integrated. The angular momentum density with respect to the $R\theta$ coordinate is given by

$$L_{\text{density}} = 2\pi(R \sin \theta)^2 \Sigma(\partial \bar{\xi}_\phi(\theta)/\partial t). \quad (35)$$

Angular momentum conservation demands

$$\partial(L_{\text{density}})/\partial t = -(1/R) \partial(L_{\text{flux}})/\partial \theta. \quad (36)$$

By substituting Eqs (34) and (35) into Eq. (36) and performing some trivial algebra, one obtains

$$\frac{\partial^2 \bar{\xi}_\phi(\theta)}{\partial t^2} = \omega_{\text{el}}^2 \left[\frac{\partial^2 \bar{\xi}_\phi}{\partial \theta^2} + \cot(\theta) \frac{\partial \bar{\xi}_\phi}{\partial \theta} - (\cot^2(\theta) - 1) \bar{\xi}_\phi \right], \quad (37)$$

where

$$\omega_{\text{el}}^2 = \frac{\int \mu dr}{\Sigma R^2} = \frac{\bar{\mu}/\bar{\rho}}{R^2}. \quad (38)$$

The right-hand side of Eq. (37) is the operator $L(\bar{\xi}_\phi)$ used in the text.

7 APPENDIX B: QPOS FROM EDGES AND TURNING POINTS IN THE CONTINUUM

The purpose of this Appendix is to explain mathematically the late-time behaviour of QPOs produced by the edges and turning points of the continuum in the toy models of subsection 3.1.

7.1 Edges

Lets assume that after initial excitation, the oscillation amplitude of the small pendulae described in the subsection 3.1 does not change. Then the force acting on the big pendulum can be written as

$$F(t) = \int_{\omega_{\min}}^{\omega_{\max}} d\omega f(\omega) \exp(i\omega t), \quad (39)$$

where ω_{\min} and ω_{\max} are the upper and lower edges of the continuum, and function $f(\omega)$ encompasses the amplitude of excitation, the coupling strength, and the density of the continuum states at frequency ω . Lets continue $f(\omega)$ smoothly outside the $(\omega_{\min}, \omega_{\max})$ region in such a way that $f \rightarrow 0$ sufficiently fast (to be presently specified) as $|\omega| \rightarrow \infty$. We call this new function $\tilde{f}(\omega)$ and choose it in such a way that its inverse Fourier transform, $f^*(t)$, has a finite effective width Δt . Then $F(t)$ is the convolution of $f^*(t)$ and $s^*(t)$,

$$F(t) \propto \int d\tau f^*(\tau) s^*(t - \tau). \quad (40)$$

Here

$$s^*(t) = [\exp(i\omega_{\max} t) - \exp(i\omega_{\min} t)]/t \quad (41)$$

is the inverse Fourier transform of the function $s(\omega)$, which equals 1 for $\omega_{\min} < \omega < \omega_{\max}$, and 0 otherwise. When $t \gg \Delta t$, we can substitute $1/(t - \tau)$ with $1/t$ in Eq. (40). Then we have for late times

$$F(t) \propto [f(\omega_{\max}) \exp(i\omega_{\max} t) - f(\omega_{\min}) \exp(i\omega_{\min} t)]/t, \quad (42)$$

and thus the edge QPOs decay as $1/t$.

7.2 Turning points

Consider a downward turning point at angular frequency ω_0 (i.e., a local maximum in ω as a function of m). The density of states near the turning point scales as $(\omega_0 - \omega)^{-1/2}$. Then the contribution of the oscillators near the turning point frequency to the force acting on the big pendulum is given by

$$F(t) \propto \int_{\omega_0}^{\omega_0} d\omega (\omega_0 - \omega)^{-1/2} \exp(i\omega t). \quad (43)$$

Introducing the new variable $x = (\omega_0 - \omega)t$ and noticing that for large t the range of x becomes essentially $(-\infty, 0)$, we see that

$$F(t) \propto \left[\int_{-\infty}^0 x^{-1/2} \exp(ix) \right] \times \frac{\exp(i\omega_0 t)}{t^{1/2}}. \quad (44)$$

Thus, the amplitude of the QPO associated with the turning point decays as $t^{-1/2}$.

References

- Barat, C., et al. 1983, A&A, 126, 400
 Blaes, O., et al. 1989, ApJ, 343, 839
 Braithwaite, J., & Spruit, H. C. 2004, Nature, 431, 819
 Braithwaite, J., & Spruit, H. C. 2006, A&A, 450, 1097
 Duncan, R.C. 1998, ApJ, 498, L45
 Duncan, R.C., & Thompson, C. 1992, ApJ, 392, L9
 Glampedakis, K., Samuelsson, L., & Andersson, N. 2006, MNRAS, 371, L74 (GSA)
 Hollweg, J. 1987a, ApJ, 312, 880
 Hollweg, J. 1987b, ApJ, 320, 875
 Hurley, K., et al. 1999, Nature, 397, 41
 Hurley, K., et al. 2005, Nature, 434, 1098
 Ionson, J.A. 1978, ApJ, 226, 650
 Israel, G.L., et al. 2005, ApJ, 628, L53
 Kinoshita, H., Yoshida, H., & Nakai, H. 1991, Celest. Mech. Dyn. Astron., 50, 59
 Lee, U. 2006, accepted to MNRAS, astro-ph/0610182
 Levin, Y. 2006, MNRAS, 367, L35 (L06)
 Lyutikov, M. 2003, MNRAS, 346, 540
 Mazets, E.P., et al., Nature, 282, 587
 Piro, A.L. 2005, ApJ, 634, L153
 Rincon, F., & Rieutord, M. 2003, A&A, 398, 663
 Reese, D., Rincon, F., & Rieutord, M. 2004, A&A, 427, 279
 Ruderman, M., Zhu, T., & Chen, K. 1998, ApJ, 492, 267
 Samuelsson, L., Andersson, N. 2006, astro-ph/0609265
 Sotani, H., Kokkotas, K.D., & Stergioulas, N. 2006, astro-ph/0608626 (s06a)
 Sotani, H., Kokkotas, K.D., & Stergioulas, N., Vavoulidis, M. 2006, astro-ph/0611666 (s06b)
 Steinolfson, R.S. 1985, ApJ, 295, 213
 Strohmayer, T.E., & Watts, A.L. 2005, ApJ, 632, L111
 Strohmayer, T.E., & Watts, A.L. 2006, ApJ, 653, 594
 Watts, A.L., & Strohmayer, T.E. 2006, ApJ, 637, L117
 Watts, A.L., & Reddy, S. 2006, submitted to Phys. Rev. Letters, astro-ph/0609364